Ecotoxicology and Environmental Safety 326 (2026) 120984

Contents lists available at ScienceDirect

Ecotoxicology and Environmental Safety

journal homepage: www.elsevier.com/locate/ecoenv

Integrated assessment of mercury-tolerant plant-associated bacteria from a chlor-alkali site identifies candidates for bioaugmentation

Lorraine Meyer [a], Jun Zhou [b,*], Stéphane Pfendler [b], Akanksha Mishra [c], Lila Otero-Gonzalez [c], Marta Franco-Benito [c], Sara Gil-Guerrero [c], Alexandre Meunier [d], Didier Hocquet [a,d], Stéphane Guyot [e], Nicolas Capelli [a], Michel Chalot [b]

[a] Université Marie et Louis Pasteur, CNRS, Chrono-environnement (UMR 6249), Besançon, F-25000, France
[b] Université Marie et Louis Pasteur, CNRS, Chrono-environnement (UMR 6249), Montbéliard, F-25200, France
[c] IDENER.AI, Biotechnology Division, C/ Gonzalo Jimenez de Quesada, 2, Tower, Floor 11, Seville, 41092, Spain
[d] CHU Besançon Franche-Comté, Hygiène Hospitalière, Besançon, F-25000, France
[e] Université Bourgogne Europe, Institut Agro, INRAE, UMR PAM, Dijon, F-21000, France

ARTICLE INFO

Keywords:
Functional screening
Genome-scale metabolic modelling
Metal tolerance
Microbial consortia
Rhizosphere

ABSTRACT

Mercury (Hg)-contaminated environments harbour microorganisms with traits that may be useful for plant-assisted remediation, but high Hg tolerance alone may not identify the most suitable strains for inoculation. In this study, plant-associated bacteria isolated from a chlor-alkali site were evaluated through phenotypic screening, whole-genome analysis, genome-scale metabolic modelling, and willow inoculation assays. Fifty-one Hg-tolerant isolates were recovered, of which 16 were selected for detailed characterization. All selected isolates displayed at least one plant growth-promoting trait, including indole-3-acetic acid production, siderophore production, or phosphate solubilization. *Pseudomonas canadensis* UFC_B020 and *Pseudomonas umsongensis* UFC_B021 grew at 200 μM Hg, the highest concentration tested. Genome-based analyses identified putative functions related to metal transport, membrane efflux, oxidative stress responses and plant-beneficial metabolism, while community-scale modelling predicted potential metabolite exchanges within three selected bacterial consortia. In willow inoculation assays, consortium 1 increased root projected area by 5.7% relative to the uninoculated control. The strongest root response was therefore associated with a different consortium from that containing the two isolates with the highest Hg tolerance, highlighting the value of considering both Hg tolerance and plant responses in candidate selection. Together, these results support an integrated strategy combining Hg tolerance, plant growth-promoting traits, genome-based functional information and consortium performance to prioritize site-derived bacteria for subsequent bioaugmentation studies.

1. Introduction

Human activities have increased the release of mercury (Hg), one of the most toxic pollutants, ranked by the World Health Organization among the 10 compounds of major public concern for human health (Meyer et al., 2023). Indeed, Hg induces oxidative stress and disrupts protein functions by altering their three-dimensional structures (Rice et al., 2014). Moreover, anthropogenic activities have tripled the global atmospheric Hg deposition rates compared to preindustrial times (Xu et al., 2014).

Despite the toxicity and persistence of Hg, some microorganisms have adapted by developing resistance mechanisms. For instance, the *mer* operon mediating Hg reduction is widespread in several archaeal and bacterial taxa (Christakis et al., 2021). Among other microbial mechanisms to cope with Hg toxicity, biosorption and bioaccumulation have also been observed in bacteria through chelation by sulphur-containing compounds such as thiols or metallothioneins (François et al., 2011).

Several previous studies have focused on the isolation of Hg-resistant bacteria from contaminated environments (Priyadarshanee et al., 2021), reflecting the important role of microorganisms in the biogeochemical cycle of Hg and their potential use in bioremediation (Meyer et al., 2023). The use of biological systems or their derivatives to restore contaminated environments has therefore gained increasing interest as a

* Corresponding author.
E-mail address: jun.zhou@univ-fcomte.fr (J. Zhou).

https://doi.org/10.1016/j.ecoenv.2026.120984
Received 17 July 2026; Received in revised form 19 October 2026; Accepted 25 October 2026
Available online 28 October 2026
0147-6513/© 2026 The Author(s). Published by Elsevier Inc. This is an open access article under the CC BY license (http://creativecommons.org/licenses/by/4.0/).

cost-effective and environmentally friendly alternative to conventional remediation methods. In recent years, culture-dependent approaches have increasingly been combined with genome analysis to characterize bacterial strains with potential for bioremediation applications (Kumar et al., 2023). However, Hg tolerance alone may not be sufficient to identify the most suitable candidates for plant-associated applications, where additional functional traits and performance in bacterial consortia also need to be considered.

This study investigates whether Hg-resistant rhizospheric bacteria exhibit phenotypic, genomic and metabolic traits that could support their selection for plant-associated applications in Hg-contaminated soils. To this end, bacterial strains were isolated from the rhizosphere of plants growing at a Hg-enriched chlor-alkali site and screened for Hg tolerance. Key functional traits, including Hg minimum inhibitory concentration (MIC), plant growth-promoting (PGP) traits and resistance to antibiotics of clinical importance, were evaluated. Genomic characterization and genome-scale metabolic models (GEMs) were then used to assess their functional potential and possible metabolic complementarity. Finally, selected bacterial consortia were evaluated using *Salix aquatica grandis* to determine their effects on plant root development under controlled conditions. By comparing Hg tolerance, plant-beneficial traits, genomic and metabolic potential, and consortium-level plant responses within the same site-derived bacterial collection, this study provides an integrated basis for prioritizing candidate strains and consortia for subsequent bioaugmentation and microbe-assisted phytoremediation studies.

2. Materials and methods

2.1. Site description and rhizosphere sampling design

The location and history of the study site, along with soil physico-chemical parameters, have been described in detail elsewhere (Zappelini et al., 2015). Briefly, the site is located in Saint-Symphorien-sur-Saône, Côte d'Or, France (Latitude: 47° 5′ 5.985" North, Longitude: 5° 19' 44.0322" East), and was exploited as a storage area for Hg-contaminated sediments, with concentrations varying from 2 to 10 mg per kg of soil.

Bacterial strains of interest were isolated from soil and root samples collected in November 2022 under the canopy of several tree species (*Populus*, *Salix*, *Robinia*, and *Pterocarya*) at a depth of 20 cm. Each sample comprised three root and associated-soil subsamples collected beneath the canopy of the same tree and pooled as one composite sample. Each composite sample was collected in sterile plastic bags and then stored at 4 °C.

2.2. Isolation of Hg-resistant strains

Root samples were shaken manually to remove the excess of soil and then incubated for 30 min at 150 rpm in 10 mM $MgSO_4$ (Sigma-Aldrich, St. Louis, MO, USA) to solubilize the rhizospheric soil. Roots were then disinfected for 2 min in a 1% hypochlorite solution, rinsed 5 times in sterile distilled water, ground in PBS (Sigma-Aldrich) and incubated for one hour of maceration with agitation at 100 rpm. The rhizospheric soil and root solutions were diluted in PBS to 10^{-3} and 10^{-2}, respectively, and then plated on 284 agar medium, prepared as described in Becerra-Castro et al. (2011), supplemented with 0.05 g/L cycloheximide (Euromedex, Souffelweyersheim, France) and 10 μM Hg, a concentration close to that of the study site, to isolate Hg-resistant bacterial strains. After 48 h of incubation at 30 °C, individual colonies were picked and subcultured to obtain pure isolates, with the medium still supplemented with 10 μM Hg.

2.3. Identification of bacterial isolates

All bacterial isolates were screened by Matrix-Assisted Laser Desorption Ionization Time-Of-Flight Mass Spectrometry (MALDI-TOF MS, Microflex, Bruker, Bremen, Germany) to discriminate against potential duplicates among isolates (Santos et al., 2016). Bacteria were cultured on 284 agar plates for 24 h at 30 °C and identified using MALDI-TOF MS following the manufacturer's instructions.

Following MALDI-TOF MS screening, bacterial DNA was extracted as described in Zappelini et al. (2015) using the E.Z.N.A.® Bacterial DNA kit (Omega Bio-Tek, Inc., Norcross, GA, USA). Extracted DNA was then quantified using the Qubit™ dsDNA HS Assay Kit (Invitrogen, Carlsbad, CA, USA) and the A260/A230 and A260/A280 ratios were measured with the Spark® microplate reader (Tecan, Männedorf, Switzerland) to check the quality of the DNA extracts.

Bacterial strains were identified by 16S rRNA sequencing. Variable regions V1 to V9 were amplified with primers 27 F (5' AGAGTTTGATCCTGGCTCAG 3') and 1492 R (5' ACGGTTACCTTGTTACGACTT 3') (Frank et al., 2008). Amplifications were performed following the protocol described in Zappelini et al. (2015). Amplicon specificity was checked by separation on a 1% agarose gel for 30 min at 75 V, before Sanger sequencing by Genewiz-Azenta (Leipzig, Germany). Identification was carried out by aligning the sequences obtained using the BLASTn tool on the NCBI website (https://blast.ncbi.nlm.nih.gov/Blast.cgi, accessed on 18/04/2025).

2.4. Phenotypic characterization of bacterial isolates

2.4.1. Determination of Hg minimum inhibitory concentration

In order to determine the MIC of Hg for the bacterial isolates, growth tests were performed in 96-well plates containing solutions of increasing concentrations of Hg, prepared in Luria-Bertani broth (LBB): 0, 10, 25, 50, 75, 100, and 200 μM. The bacteria were pre-cultured in LBB containing 10 μM Hg overnight at 30 °C and 250 rpm until stationary growth phase. The 96-well plates containing in each well 200 μL of LBB supplemented with Hg were then inoculated with the pre-cultured bacteria. Four replicates were performed for each concentration tested. The inoculated 96-well plates were incubated for 48 h at 30 °C under agitation (250 rpm). At the end of the incubation period, the optical density at 600 nm (OD_{600}) was measured in each well using the Spark® microplate reader.

2.4.2. PGP assays

All assays were performed in 96-well plates. Bacterial strains were pre-cultured in LBB overnight at 30 °C and 250 rpm until stationary phase. After incubation, the OD_{600} of cultures was adjusted to 1 using a 9 g/L KCl solution (Sigma-Aldrich).

For siderophore production, 225 μL of Casamino acids medium (Sigma-Aldrich) was inoculated with 25 μL of bacterial culture (four replicates per strain) and incubated for 3 days at 30 °C and 250 rpm. After centrifugation (20 min, 2000 rpm), 15 μL of supernatant was diluted in 135 μL ultrapure water, mixed with 150 μL CAS reagent (Schwyn and Neilands, 1987), and incubated for 2 h in the dark at 25 °C. OD_{630} was measured, and siderophore production was quantified using a DFOM standard curve, normalized to biomass.

For indole-3-acetic acid (IAA) production, 25 μL of 5 g/L L-tryptophan (Sigma-Aldrich) and 200 μL of DF minimal medium (Dworkin and Foster, 1958) supplemented with 10 g/L glucose were inoculated with 25 μL of bacterial culture. After 3 days of incubation, plates were centrifuged, and 50 μL of supernatant was mixed with 200 μL Salkowski reagent (Gang et al., 2019). After 1 h in the dark at room temperature, OD_{541} was measured, and IAA production was quantified using an IAA standard curve, normalized to biomass.

For phosphate solubilization, 225 μL of modified NBRIY medium (Nautiyal, 1999) was inoculated with 25 μL of pre-culture. After incubation and centrifugation, 150 μL of supernatant was mixed with 150 μL nitrovanadomolybdic reagent (Sigma-Aldrich) (Braud et al., 2015). After 1 h in the dark at room temperature, OD_{450} was measured. Pellets were resuspended in 150 μL of 6 N HCl to dissolve remaining phosphate,

and OD_{600} was measured to assess bacterial growth. Phosphate solubilization was quantified using a K_2HPO_4 standard curve, normalized to biomass.

2.4.3. Determination of antimicrobial resistance profiles

We tested the resistance of each bacterial isolate to antibiotics of clinical importance using the disc diffusion method. Isolates were thawed on LB agar supplemented with Hg 10 μM and plates were incubated 24 h at 30 °C. A single colony was suspended in sterile water to a 0.5 McFarland turbidity (corresponding to approximately 10^8 CFU/mL) and spread with a sterile swab onto Müller-Hinton agar plates (Sigma-Aldrich). Susceptibility to clinically relevant antibiotics was tested using the following antibiotic disks (Bio-Rad, Marnes-la-Coquette, France): cefepime (30 μg), ceftazidime–avibactam (10/4 μg), piperacillin–tazobactam (30/6 μg), cefotaxime (30 μg), ticarcillin–clavulanic acid (75/10 μg), ceftazidime (10 μg), meropenem (10 μg), imipenem (10 μg), tobramycin (10 μg), aztreonam (30 μg), ceftolozane–tazobactam (30/10 μg), ciprofloxacin (5 μg), amikacin (30 μg), levofloxacin (5 μg), and trimethoprim–sulfamethoxazole (1.25/23.75 μg). Plates were incubated for 24 h at 30 °C. Inhibition zone diameters were interpreted using European Committee on Antimicrobial Susceptibility Testing breakpoints (EUCAST, version 15.0, 2025).

2.5. Whole-genome sequencing and variant analysis

After identification of the isolates, genomic DNA was extracted using the same procedure as for Sanger sequencing, and the genomes of selected strains were sequenced by whole-genome sequencing (WGS). Libraries were constructed following the standard Illumina protocol: high-molecular-weight DNA was sheared by ultrasonication, fragment-purified, end-repaired, 3′-A tailed, and ligated to Illumina sequencing adapters. Size selection was performed on agarose gels, followed by limited-cycle PCR amplification to generate the final libraries. Libraries underwent quality control and, if meeting acceptance criteria, were sequenced on an Illumina NovaSeq 6000 platform (Illumina, San Diego, CA, USA). Clean reads (adapter-trimmed and quality-filtered) were aligned to the appropriate species reference genome (Table S1) using BWA (v0.7.17-r1188). Duplicate reads were identified with Picard MarkDuplicates (v2.21.2) and excluded from variant calling. Single-nucleotide polymorphisms (SNPs) and small insertions/deletions (InDels) were then called with GATK (v4.1.4.1). The functional impact of SNPs and small InDels was annotated with SnpEff (v4.3t). Genes harbouring filtered variants were functionally annotated by sequence similarity searches (BLAST) against standard databases to infer putative functions and pathway associations.

2.6. Construction of GEM

The protein sequences of each bacterial strain were taken in the.faa format. The CarveMe model reconstruction protocol was employed, which is an automated, top-down approach for building GEMs of microbial species and communities (Machado et al., 2018). CarveMe is built on a manually curated universal model of bacterial metabolism, which is derived from the BiGG database from which organism specific GEMs are reconstructed by selectively retaining reactions and metabolites supported by the annotated genome. The models were further analysed in Cytoscape v3.10.1 to visualise selected reaction and gene networks using the “Prefuse Force Directed” layout algorithm.

2.7. Exploration of metabolite exchanges and inter-species interactions within the consortia

Community metabolic interactions were analysed using the MICOM framework (Diener et al., 2020). Individual GEMs were integrated into a community model connected via a shared extracellular compartment, allowing metabolite exchange between taxa (Diener et al., 2020). Initial community growth was first computed using the cooperative trade-off optimization to estimate a consistent value for the community growth rate, from corresponding individual taxon growth rates (Table 1). All three communities had an overall average growth rate of $0.405 \pm 0.016\ h^{-1}$ ($n = 10$). Following this, the cooperative trade-off optimization was rerun for the second time to obtain steady-state flux distributions. The trade-off parameter controls how much of the maximum community growth must be preserved and selects the most “cooperative” solution among the many feasible ones (Diener et al., 2020). The resulting flux distributions were examined to identify metabolites predicted to be secreted or taken up by individual community members.

The predicted exchange metabolites were grouped into two main functional categories according to their reported roles in plant growth promotion and microbial responses to metal stress: (1) metabolites directly associated with heavy metal-induced stress tolerance mechanisms and (2) metabolites indirectly associated with stress adaptation processes. These values are shown in Tables S2, S3 and S4.

2.8. Assessment of the PGP character of bacteria in vivo

2.8.1. Design of bacterial consortia and preparation of bacterial inocula

Isolate selection followed a three-step procedure: (i) isolates identified as potential plant or human pathogens were excluded based on literature, and isolates with documented PGP traits and/or heavy-metal tolerance were retained ($n = 16$); (ii) among these, isolates were selected if they met both of the following criteria: a Hg MIC of at least 50 μM, to ensure growth in highly Hg-contaminated sediments, and at least one *in vitro* PGP trait (IAA production, siderophore production, or phosphate solubilization); (iii) the selected isolates were assigned to consortia based on pairwise compatibility assays performed as described in Barbosa et al. (2018). Only mutually compatible strains were grouped together. The resulting three consortia tested for *S. aquatica grandis* inoculation were: i) UFC_B030 + UFC_B029 + UFC_B037 (consortium 1); ii) UFC_B023 + UFC_B028 + UFC_B024 + UFC_B036 (consortium 2); iii) UFC_B041 + UFC_B020 + UFC_B021 (consortium 3). The selected bacteria were cultured in LBB overnight at 30 °C and 250 rpm until stationary growth phase. Strains mutually compatible were co-cultured as follows to obtain bacterial inocula: each bacterial culture was 100-fold diluted in autoclaved jars containing 200 mL of perlite and 200 mL of LBB and incubated for 48 h at 30 °C.

2.8.2. Plant inoculation assay on S. aquatica grandis cuttings under controlled growth-chamber conditions

S. aquatica grandis cuttings were prepared and grown as described in Collot et al. (2026) in 2 growth chambers (one for the control plants and the other for the plants inoculated with the different bacterial consortia, to avoid contamination of control plants). For each consortium tested, 15 cuttings were planted individually in one-litre pots containing the bacterial inoculum diluted 10 times in sterilized perlite. The control cuttings were planted in sterilized perlite only.

Once a week, as soon as the development of the cuttings allowed it, the length of the stems was measured and the chlorophyll content of the leaves was evaluated using the Chlorophyll Content Meter 200 (Opti-Sciences, Hudson, NH, USA). After 6 weeks of cultivation, the plants were harvested, and the roots were carefully rinsed before further measurements. Total biomass, stem biomass, leaf biomass, root biomass, total stem length, total number of leaves, leaf dried mass and root dried mass (obtained after 48 h of incubation at 70 °C) were measured. Leaf and root surfaces as well as total root length were measured using the WinRhizo scanner (Regent Instrument, Quebec, Canada).

2.9. Statistical analysis

All results were analysed using the R Studio software v4.3.1. Sample sizes (n) of biological replicates are indicated in each Figure and Table

Table 1
Model attributes and communities' growth rates.

Community	Model	Abundance	Growth rate (h^{-1})	Reactions	Metabolites
1	UFC_B029	0.333	0.384	2498	1572
1	UFC_B030	0.333	0.384	2686	1692
1	UFC_B037	0.333	0.383	2588	1645
2	UFC_B023	0.250	0.419	2760	1722
2	UFC_B024	0.250	0.419	2543	1610
2	UFC_B028	0.250	0.419	2775	1788
2	UFC_B036	0.250	0.419	2498	1572
3	UFC_B020	0.333	0.408	2560	1635
3	UFC_B021	0.333	0.408	2563	1625
3	UFC_B041	0.333	0.408	2563	1627

legend. Normality was assessed with the Shapiro-Wilk test and homogeneity of variances with the Bartlett test. As the assumption of normality was not met for any dataset presented below, differences between conditions were assessed using the non-parametric Kruskal-Wallis test. When the Kruskal-Wallis test was significant (p-value $<$ 0.05), pairwise comparisons were performed using Dunn's post-hoc test with Benjamini-Hochberg correction for multiple comparisons. Conditions sharing the same letter are not significantly different (adjusted p-value $\geq$ 0.05).

3. Results

3.1. Isolation of Hg-resistant bacteria

A total of 51 Hg-resistant isolates grew on 284 agar supplemented with Hg. Following MALDI-TOF MS screening and 16S rRNA sequencing, 95% of the isolated bacteria were identified as belonging to the genus *Pseudomonas*. *Achromobacter* and *Ensifer* species were also identified. Following molecular identification, a literature search was conducted to discard potential plant and human pathogens and to guide further phenotypic characterization, focusing only on strains of interest for bioremediation applications. Based on published evidence of PGP traits and heavy metals tolerance, a total of 16 isolates were selected for downstream analyses.

3.2. Evaluation of Hg tolerance in bacterial isolates

Fig. 1 shows that all isolates grew in liquid medium supplemented with Hg at 10 μM. No growth difference was observed between 0 and 10 μM Hg, which is not surprising given that the strains were initially isolated on agar medium supplemented with 10 μM Hg during the screening for resistant bacteria from rhizosphere samples. However, at higher concentrations, fewer isolates were able to grow, indicating differences in Hg tolerance. Only UFC_B020 (*Pseudomonas canadensis*) and UFC_B021 (*P. umsongensis*) strains exhibited growth at 200 μM while a concentration of 50 μM appeared to be a threshold beyond which three-quarters of the bacteria were no longer able to develop.

3.3. Assessment of PGP character in vitro

Bacterial isolates were screened to evaluate PGP traits *in vitro*. Indeed, the presence of these phenotypical features could potentially stimulate plant growth and optimize revegetation strategies of contaminated areas. The first PGP parameter evaluated in bacterial isolates was the IAA production, which is one of the most widespread phytohormones, with concentration-dependent effects at different stages of plant development. According to Fig. 2**A**, all strains produced IAA, albeit in varying quantities. For instance, strain UFC_B029 was the biggest producer (0.58 mM), unlike strain UFC_B042, whose production was extremely low (0.11 mM). The screening for siderophore-producing strains identified UFC_B039, UFC_B041, UFC_B042 and UFC_B045 as positive producers, whereas no siderophore production could be

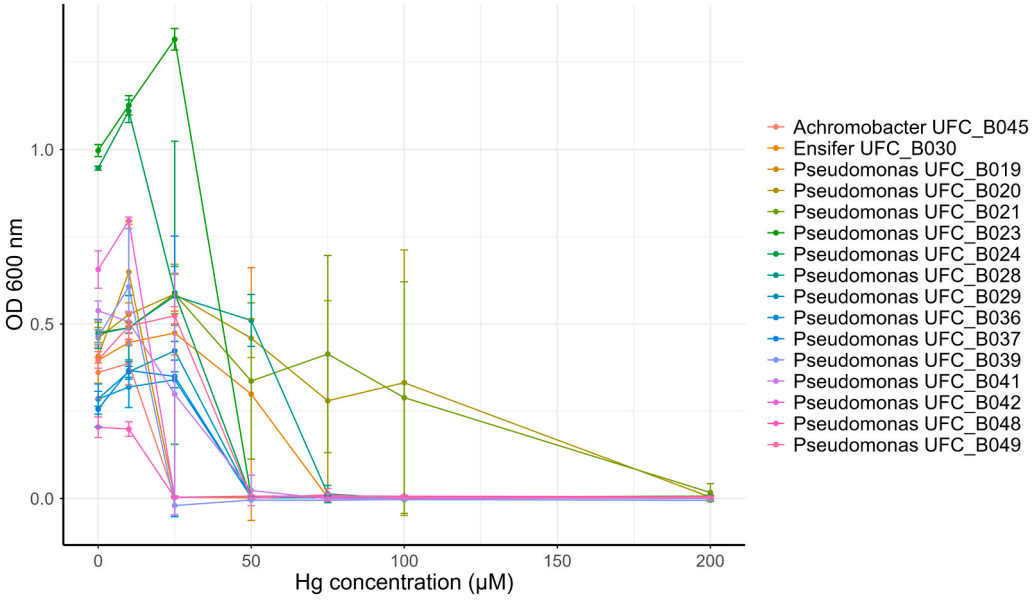


Fig. 1. Growth curves of bacterial isolates at increasing Hg concentrations. Bacterial growth (OD_{600}) was measured in the culture medium after 48 h incubation at 30 °C. Error bars represent standard deviation (n = 4).

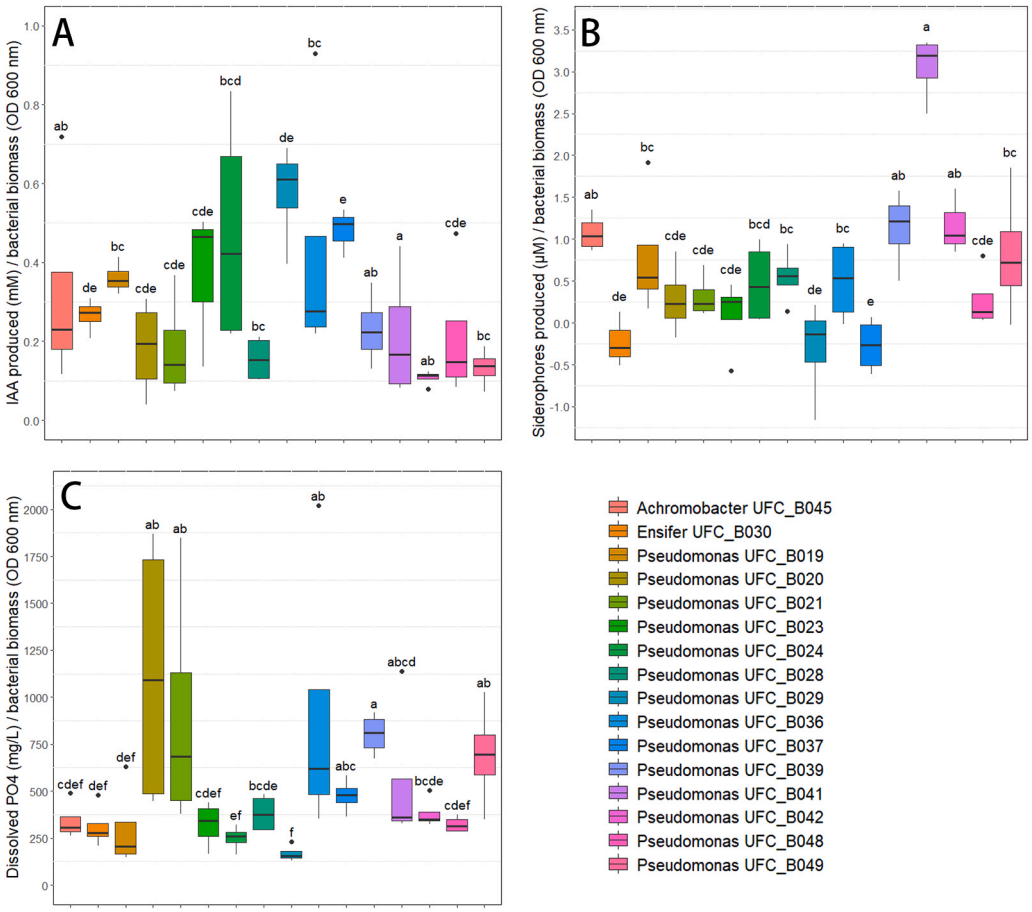


Fig. 2. **(A)** Production of IAA (mM) relative to bacterial biomass (OD_{600}). **(B)** Production of siderophores (µM) relative to bacterial biomass (OD_{600}). **(C)** Solubilization of phosphate (mg/L) relative to bacterial biomass (OD_{600}). Letters indicate significant differences between strains according to Kruskal-Wallis test followed by Dunn analysis ($p < 0.05$ and $n = 4$).

detected in UFC_B029, UFC_B030 and UFC_B037 under the conditions tested (Fig. 2**B**). UFC_B041 stood out as the best siderophore producer with values almost 3 times higher than other strains. Finally, the ability of the strains to solubilize phosphate was assessed: all the strains appeared to be capable of solubilizing phosphate, as displayed on Fig. 2**C**. Strains UFC_B020 and UFC_B021 emerged as the most efficient phosphate solubilizers, although they exhibited high variability. Similar to siderophore production, and in contrast to IAA production, strain UFC_B029 showed only a low capacity for phosphate solubilization. Together, these results confirm that certain isolated strains exhibit traits relevant to stimulating plant growth, particularly in contexts of heavy metal stress, either alone or in combination within a consortium.

3.4. Resistance of Hg-resistant bacteria to clinically relevant antibiotics

The susceptibility of bacterial strains to various antibiotics was assessed and the diameters of the zones of inhibition for each antibiotic tested are detailed in Table S5 and Table S6. The bacteria were divided into two groups, with different types of antibiotics tested for each group: bacteria belonging to the *Pseudomonas* genus and non-fermenting bacteria (UFC_B030 and UFC_B045). These environmental species are known to be intrinsically resistant to some antibiotics but according to the criteria for multidrug resistance defined by Barbier & Wolff (2010), a strain is considered multidrug-resistant if it exhibits resistance to at least three of the following classes of antibiotics: aminoglycosides, fluoroquinolones, carbapenems, or beta-lactams (excluding carbapenems). In this study, no resistance to aminoglycosides or fluoroquinolones was observed. Regarding carbapenems, three strains showed resistance to meropenem but not to imipenem, suggesting the absence of a carbapenemase or class D beta-lactamase resistance mechanism. Furthermore, no profile suggestive of extended-spectrum beta-lactamase was detected. All isolates displayed a wild-type antimicrobial susceptibility profile for the antibiotics evaluated.

3.5. WGS and genomic variation

3.5.1. SNP and InDel identification and annotation

Having established the phenotypic profiles, we next investigated the genomic basis of Hg tolerance and PGP traits. Whole-genome resequencing of the 16 bacterial isolates yielded 10.25–14.05 million clean reads per isolate, with Q30 values ranging from 92.11% to 95.19% (Table S7). The proportion of reads mapped to their reference genomes ranged from 70.61% (UFC_B041) to 96.62% (UFC_B049), with a median mapping rate of 85.07%. Mean sequencing depth across the full reference genomes ranged from 194.94 × to 300.23 × , while the proportion of reference positions covered at ≥ 10 × ranged from 68.48% to 94.81%. In total, 2640,053 SNPs and 100,346 InDels were identified across all isolates, corresponding to an average of 165,003 SNPs and 6272 InDels per genome. The highest SNP counts were detected in UFC_B030 (303,812), UFC_B039 (295,258), and UFC_B019 (288,961), whereas UFC_B049 displayed the lowest number of variants (6910 SNPs and 302 InDels). In general, isolates with higher mapping rates (≥89%), such as UFC_B049, UFC_B036, UFC_B020, UFC_B024, UFC_B042, and UFC_B029, harboured relatively fewer variants, while those with lower mapping rates, including UFC_B030, UFC_B039, UFC_B019, and UFC_B041, showed markedly higher SNP and InDel counts. These

patterns suggest differences in genetic divergence among isolates relative to the chosen reference genome.

Functional annotation of SNP- and InDel-bearing genes revealed that most variants were associated with biological processes relevant to Hg detoxification and stress adaptation. Variant genes were categorized into four major functional groups: *mer* operon, Czc/Cop/Znt-type transport systems, redox/antioxidant processes, and membrane and efflux functions (Fig. 3**A**). The paired heatmap clearly distinguished the contributions of SNPs and InDels to each category across the 16 isolates. SNP- and InDel-associated genes occurred in all four functional categories, with membrane and efflux functions accounting for the largest counts in both groups. To capture the overall distribution of variant types, we compared the SNP and InDel mutation loads across isolates (Fig. 3**B**). The bubble chart revealed substantial variability in the relative contribution of SNPs and InDels. Isolates such as UFC_B030, UFC_B039, and UFC_B019 harboured the largest total numbers of Hg resistance related variants, exhibiting balanced contributions from both mutation types, whereas UFC_B049 and UFC_B036 were dominated by SNPs. The network analysis (Fig. 3**C**) further highlighted that both mutation types converged on shared functional modules: metal transport, membrane integrity, and redox control, forming interconnected functional clusters.

3.5.2. *Functional enrichment of variant-associated genes*

Functional enrichment analysis of variant-associated genes revealed both common and distinct patterns for SNPs and InDels (Fig. 4). Across SNP-associated genes, the most recurrent pathways included ABC transporters, two-component systems, and branched-chain amino acid degradation, each detected in more than ten isolates (Fig. 4**A**). Additional frequently enriched categories were bacterial chemotaxis and quorum sensing, indicating pervasive variation in regulatory and signaling pathways that support rhizosphere adaptation. The bubble plot further showed that these pathways combined broad prevalence with relatively high enrichment factors (Fig. 4**B**). For InDel-associated genes, recurrent pathways were less numerous and occurred at lower frequencies compared with SNPs. The most enriched categories were again ABC transporters, two-component systems, and fatty acid degradation, but only a subset of isolates carried significant variation in these functions (Fig. 4**C**). Nevertheless, the bubble plot indicated that certain InDel-associated pathways, although restricted to fewer strains, exhibited relatively high enrichment factors, indicating isolate-specific variation (Fig. 4**D**). Taken together, these results show broad pathway representation among SNP-associated genes and more restricted patterns among InDel-associated genes.

To further explore the functional spectrum affected by genomic variation, GO enrichment analysis was performed. The comparison of significantly enriched terms in the Molecular Function and Biological Process categories revealed both convergent and distinct trends between mutation types (Fig. S1). Across the Biological Process ontology (Fig. S1A), the most frequently enriched terms involved transmembrane transport, response to oxidative stress, and metal ion homeostasis, all detected in multiple isolates. These categories include functions

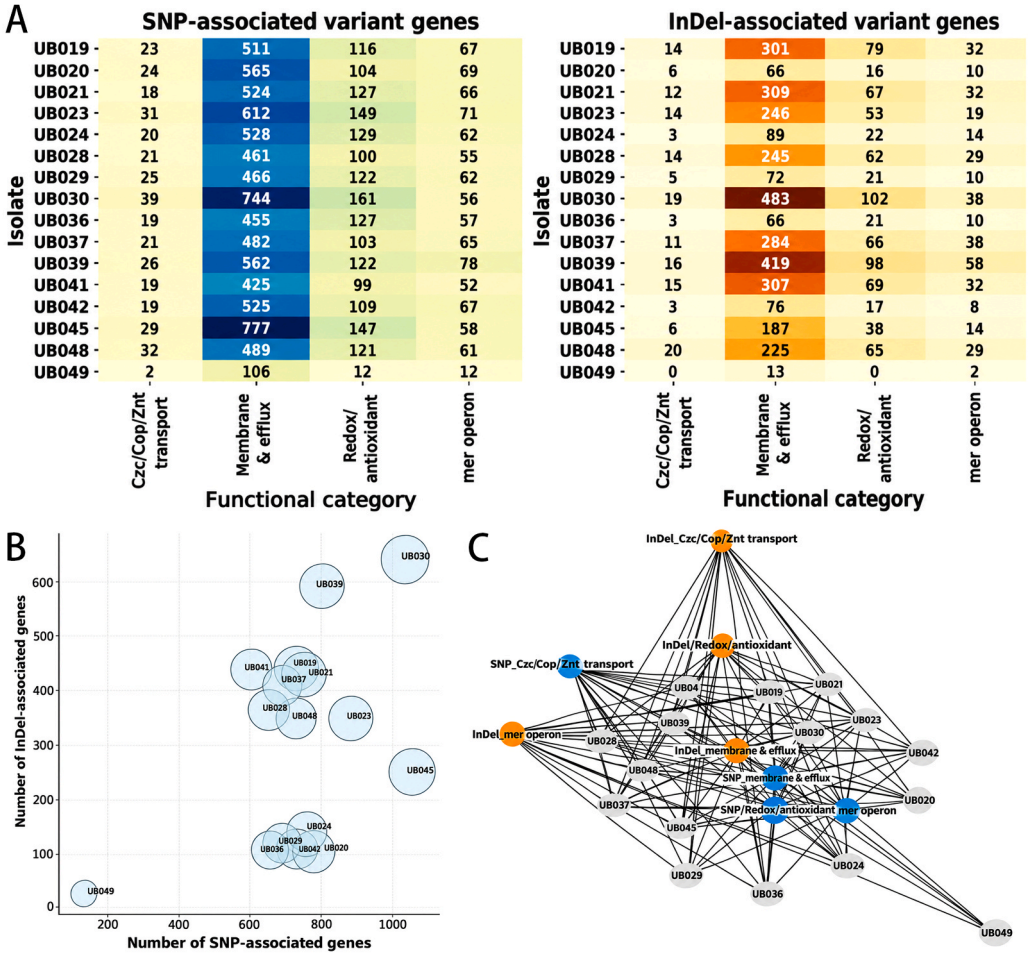


Fig. 3. Integrated functional and variant-type patterns of Hg-resistance genes across 16 bacterial isolates. **(A)** Paired heatmap showing the number of SNP- (left) and InDel-associated (right) variant genes per functional category in each isolate. **(B)** Bubble chart showing SNP versus InDel variant loads across isolates (bubble size = total number of Hg resistance-related variant genes). **(C)** Network diagram linking isolates (grey nodes) to functional categories (coloured by variant type: blue = SNP; orange = InDel).

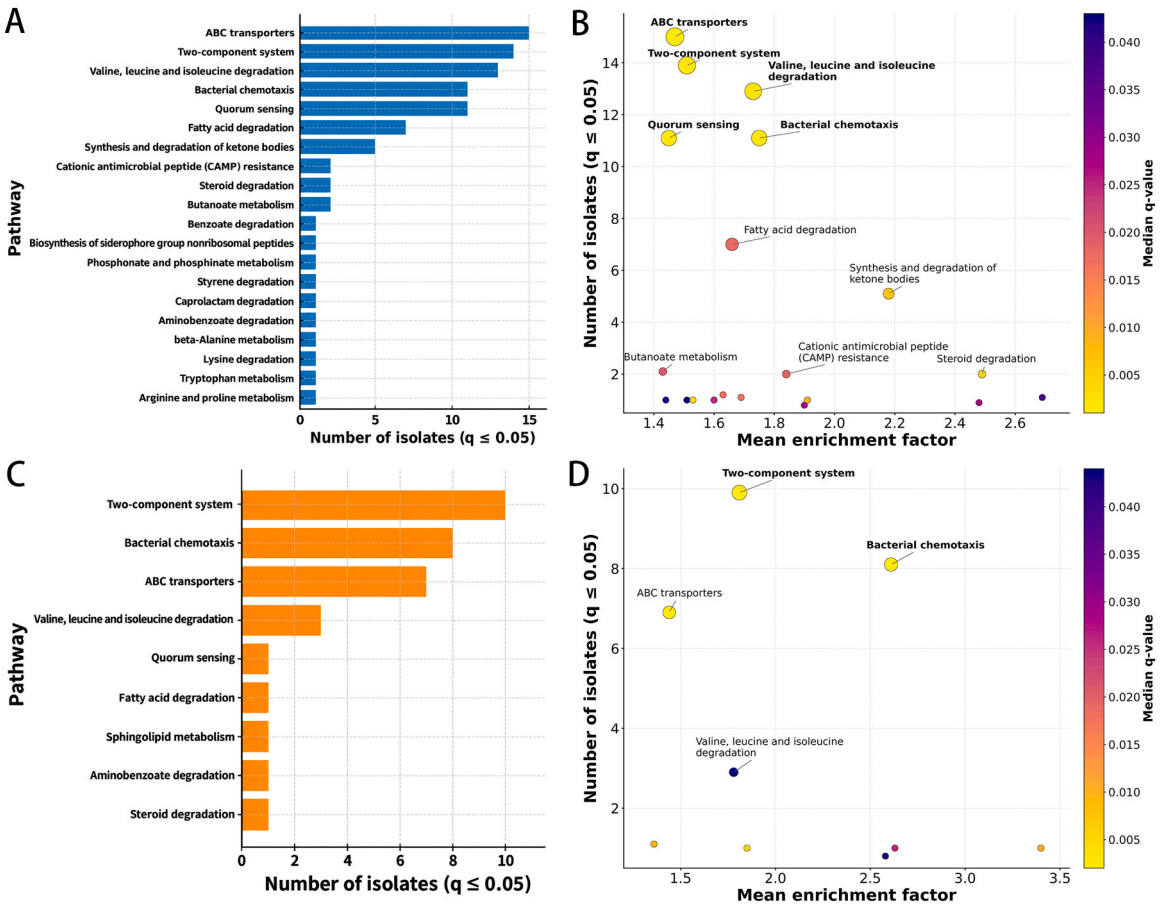


Fig. 4. KEGG enrichment of variant-associated genes across 16 isolates. **(A)** Frequency of significantly enriched pathways among SNP-associated genes ($q \leq 0.05$). **(B)** Bubble plot of SNP-associated pathways showing mean enrichment factor (x-axis) versus number of isolates (y-axis). Bubble size represents the median number of genes, and color encodes the median q-value. Only pathways detected in ≥ 2 isolates are labeled. **(C)** Frequency of significantly enriched pathways among InDel-associated genes ($q \leq 0.05$). **(D)** Bubble plot of InDel-associated pathways showing mean enrichment factor (x-axis) versus number of isolates (y-axis).

potentially relevant to survival in Hg-contaminated rhizospheres. Additional enriched terms, such as cellular response to toxic substances and protein folding, were mainly associated with SNP variants. Within the Molecular Function ontology (Fig. S1B), genes bearing SNPs and InDels were enriched in oxidoreductase activity, ATP-binding, and metal ion binding, consistent with enzymatic systems mediating Hg detoxification and redox balance. InDels were relatively less frequent but tended to occur in genes encoding membrane transporters or peroxidases.

3.5.3. *Genome-scale metabolic modelling*

Building on the functional enrichment analyses, GEM exploration enabled a more targeted investigation of metabolic functions potentially associated with heavy metals, including reactions and genes involving Hg as a metabolite, as well as the analysis of pathways related to the biosynthesis of IAA and other bioactive or biosynthetic molecules relevant to microbial adaptation and plant–microbe interactions. Exploration of the metabolic models of the 16 bacterial isolates enabled the identification of several genes associated with metal transport and resistance (Fig. 5**A** and Table S8). Among the recurrent genes associated with metal homeostasis were *fieF*, encoding a CDF-family metal efflux transporter, and *copZ*, encoding a copper chaperone. Additionally, *zosA*, *silP*, and *zntA* were detected in specific strains (UFC_B019, UFC_B023, and UFC_B030) and are linked to the transport of zinc, silver, cadmium, and Hg ions. Notably, the *zntA* gene, annotated as a lead, cadmium, zinc, and Hg-transporting P-type ATPase, was detected in two strains (UFC_B030 and UFC_B045), suggesting potential Hg efflux capacity. Interestingly, the strains exhibiting the highest Hg resistance did not consistently harbour Hg-related functions in the metabolic models. Additionally, genome-scale models often struggle to capture the complexity of metal transport mechanisms; Such reactions move "Fe^{2+}", "Zn^{2+}", "Cu^{2+}" with ATP, even though in cells these metals might be chaperoned, complexed, or moved by multi-protein systems. Furthermore, transporter annotations often have a broad substrate specificity. Hence, identifying a heavy-metal transporter therefore does not, by itself, establish mercury transport activity. In bacteria carrying the *mer* system such as in UFC_B019, detoxification also involves coordinated mercury binding, membrane transfer and intracellular reduction to Hg^0, rather than a simple export reaction.

Using the constructed GEM for UFC_B029, the pathways and reactions involved in IAA production were analysed. Bacteria synthesize IAA primarily through tryptophan-dependent pathways, beginning with tryptophan uptake and conversion into intermediates such as indole-3-acetamide and tryptamine (Zhang et al., 2021). Fig. 5**B** illustrates the interconnected reactions and metabolites, including tryptophan conversion via tryptophan transaminase (R_TRPTA), followed by intermediate steps catalysed by tryptamine oxidoreductase (R_TRYPTAOX), and aldehyde dehydrogenase (R_ALDD/R_ALDD20x). The final step involves periplasmic export of IAA (R_IND3ACtp). These modelling results are consistent with the experimental phenotypic assays, in which UFC_B029 exhibited the highest *in vitro* IAA production among the analysed isolates.

All models exhibited the biosynthetic potential for riboflavin (vitamin B_2) production, as represented in Fig. 5**C** to varying extents of the pathway. The reconstructed models contained reactions associated with de novo riboflavin biosynthesis from GTP- and ribulose-5-phosphate-derived precursors. The pathway converges at lumazine

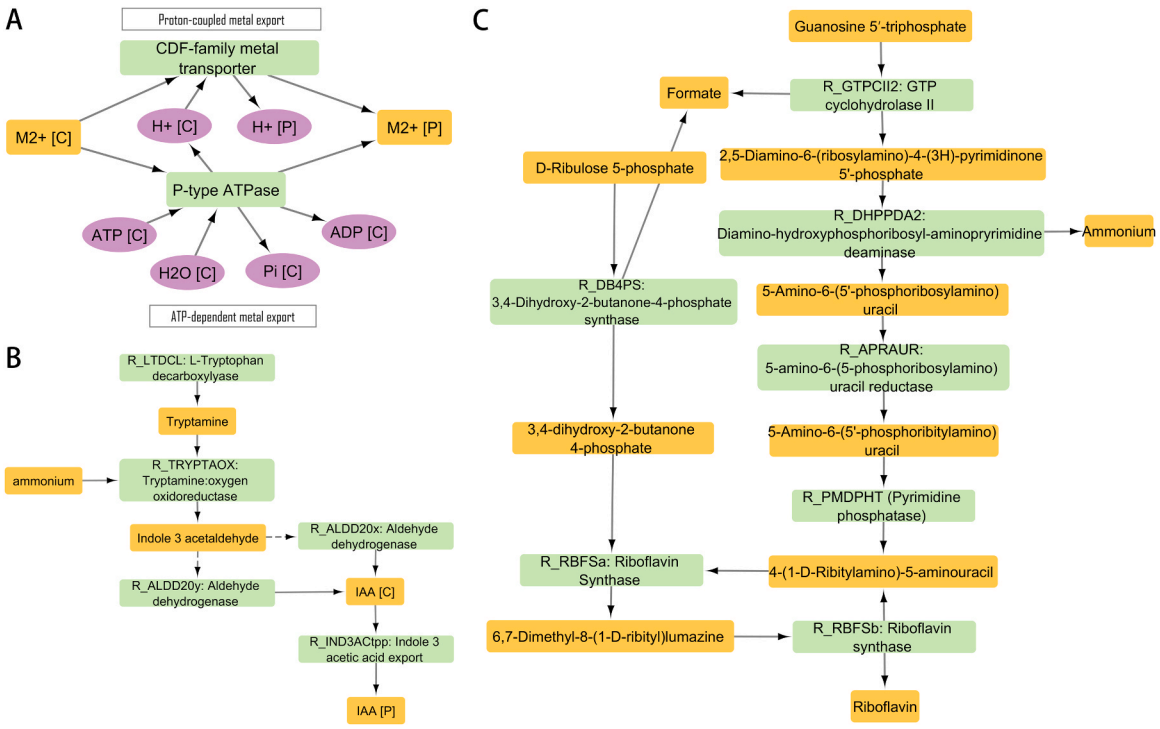


Fig. 5. Representative metabolic pathways and transport reactions identified in the reconstructed genome-scale metabolic models. **(A)** Reconstructed metal export mechanisms, including proton-coupled transport mediated by a CDF-family metal transporter and ATP-dependent export through a P-type ATPase, illustrating transport of a divalent metal ion (M^{2+}) between the cytosolic [C] and periplasmic [P] compartments. **(B)** Reconstructed tryptophan-dependent IAA biosynthesis in UFC_B029 *via* the tryptamine pathway, involving conversion of L-tryptophan to tryptamine and subsequently to indole-3-acetaldehyde and IAA, followed by transport of IAA to the periplasm. **(C)** Reconstructed riboflavin biosynthesis pathway in UFC_B028, showing the formation and convergence of the ribulose-5-phosphate- and guanosine-5′-triphosphate-derived branches leading to riboflavin production. Metabolites are shown in yellow, reconstructed reactions/enzymatic steps in green, and the reaction-associated cofactors or secondary metabolites in purple (only for panel A). Arrows indicate the directionality encoded in the reconstructed model. The pathways represent the putative metabolic functions recovered during genome-scale model reconstruction. Gene-protein-reaction associations for **(B)** and **(C)** supporting the reconstructed reactions are provided in Table S12.

intermediates before the formation of riboflavin, which can subsequently be converted into the flavin cofactors FMN and FAD. Gene–-protein–reaction associations for the terminal riboflavin synthesis reaction are listed in Table S9, while those for the pathway shown in Fig. 5**C** are provided in Table S12. The models support its metabolic potential based on the reconstruction and the gene-protein-reaction evidence, but the figure itself does not establish pathway activity. Nevertheless, these results are aligned with the widespread PGP potential observed experimentally across the isolates, as riboflavin production has been associated with plant growth promotion and stress adaptation in rhizospheric bacteria. Overall, metabolic modelling complemented variant analysis and phenotypic characterisation of strains, suggesting the potential of certain bacterial isolates for bioremediation purposes.

3.6. *Selection of relevant bacterial isolates for bioremediation applications*

All the characterization data are gathered in Table 2. Based on these results, the most relevant bacterial candidates for plant rhizospheric inoculation tests were selected among isolates. The parameters considered were as follows: i) MIC at least 50 μM, as the aim was to select only strains capable of growing in sediments highly contaminated with Hg; ii) Presence of at least one PGP trait *in vitro*, to promote plant growth *in situ* despite the presence of Hg. The 10 selected isolates having demonstrated potential for bioremediation approaches are highlighted in bold type in Table 2.

3.7. *Impact of bacterial rhizospheric inoculation on S. aquatica grandis growth*

Some strains gave positive results for PGP tests such as IAA and siderophore production or phosphate solubilization: to validate these results *in vivo* for future bioaugmentation applications, bacterial consortia were inoculated into the rhizosphere of *S. aquatica grandis*. This species was selected for inoculation tests because of the perennial growth habit of the *S. aquatica grandis*, its ease of vegetative propagation, rapid growth and robustness, which makes it a relevant plant model for bioremediation perspectives (Ciadamidaro et al., 2019). In addition, this species has been planted on the study site previously, and microbial bioaugmentation approaches using strains of interest could improve plant biomass development.

The most relevant bacterial candidates for plant rhizospheric inoculation tests were selected among isolates through characterization tests gathered in Table 2. The 10 selected isolates having demonstrated potential for bioremediation approaches are highlighted in bold type in Table 2. Individually, these isolates have appeared relevant for plant inoculation for bioremediation implementation in view of their PGP characteristics. However, within a consortium, the respective effects of the strains may be enhanced. Based on the phenotypic characterization and pairwise compatibility assays (Table S10), three bacterial consortia were selected for *S. aquatica grandis* inoculation: i) *E. adhaerens* UFC_B030 + *P. frederiksbergensis* UFC_B029 + *P. jessenii* UFC_B037 (consortium 1); ii) *Pseudomonas sp.* UFC_B023 + *P. donghuensis* UFC_B028 + *P. putida* UFC_B024 + *Pseudomonas sp.* UFC_B036 (consortium 2); iii) *P. baetica* UFC_B041 + *P. canadensis* UFC_B020 + *P. umsongensis* UFC_B021 (consortium 3).

Table 2
Summary of characterization results obtained for isolated microorganisms. Relevant candidates for bioremediation are in bold letters. The mean value ± the standard deviation is specified for each parameter (n = 4).

Designation	Taxonomic assignation	Origin	MIC (in µM of Hg)	Siderophore production (in µM) related to the biomass	IAA produced (in mM) related to the biomass	Phosphate solubilized (in g/L) related to the biomass
Achromobacter UFC_B045	*Achromobacter sp.*	Rhizospheric soil of *Populus*	25	0.20 ± 0.12	0.32 ± 0.27	0.34 ± 0.10
***Ensifer* UFC_B030**	***Ensifer adhaerens***	**Rhizospheric soil of *Salix***	**75**	**0.19 ± 0.16**	**0.27 ± 0.04**	**0.31 ± 0.12**
Pseudomonas UFC_B019	*Pseudomonas fluorescens*	Roots of *Populus*	25	0.68 ± 0.25	0.36 ± 0.04	0.30 ± 0.22
***Pseudomonas* UFC_B020**	***Pseudomonas canadensis***	**Roots of *Pterocarya***	**200**	**0.31 ± 0.24**	**0.18 ± 0.12**	**1.12 ± 0.76**
***Pseudomonas* UFC_B021**	***Pseudomonas umsongensis***	**Roots of *Pterocarya***	**200**	**0.10 ± 0.03**	**0.18 ± 0.13**	**0.90 ± 0.67**
***Pseudomonas* UFC_B023**	***Pseudomonas sp.***	**Rhizospheric soil of *Pterocarya***	**50**	**0.05 ± 0.004**	**0.37 ± 0.20**	**0.32 ± 0.12**
***Pseudomonas* UFC_B024**	***Pseudomonas putida***	**Rhizospheric soil of *Pterocarya***	**50**	**0.14 ± 0.03**	**0.47 ± 0.30**	**0.25 ± 0.07**
***Pseudomonas* UFC_B028**	***Pseudomonas donghuensis***	**Roots of *Salix***	**75**	**0.13 ± 0.009**	**0.16 ± 0.06**	**0.38 ± 0.10**
***Pseudomonas* UFC_B029**	***Pseudomonas frederiksbergensis***	**Roots of *Salix***	**50**	**0.10 ± 0.04**	**0.58 ± 0.13**	**0.17 ± 0.04**
***Pseudomonas* UFC_B036**	***Pseudomonas sp.***	**Rhizospheric soil of *Salix***	**50**	**0.06 ± 0.02**	**0.43 ± 0.34**	**0.90 ± 0.76**
***Pseudomonas* UFC_B037**	***Pseudomonas jessenii***	**Rhizospheric soil of *Pterocarya***	**50**	**0.06 ± 0.004**	**0.48 ± 0.06**	**0.48 ± 0.09**
Pseudomonas UFC_B039	*Pseudomonas protegens*	Rhizospheric soil of *Pterocarya*	25	0.24 ± 0.05	0.23 ± 0.09	0.80 ± 0.11
***Pseudomonas* UFC_B041**	***Pseudomonas baetica***	**Rhizospheric soil of *Salix***	**50**	**0.19 ± 0.09**	**0.21 ± 0.17**	**0.55 ± 0.39**
Pseudomonas UFC_B042	*Pseudomonas sp.*	Rhizospheric soil of *Salix*	25	0.12 ± 0.05	0.11 ± 0.02	0.38 ± 0.08
Pseudomonas UFC_B048	*Pseudomonas fluorescens*	Rhizospheric soil of *Populus*	25	0.09 ± 0.02	0.21 ± 0.18	0.32 ± 0.04
Pseudomonas UFC_B049	*Pseudomonas sp.*	Roots of *Populus*	50	0.16 ± 0.02	0.13 ± 0.05	0.69 ± 0.28

No significant differences were observed between the control seedlings and the different inoculation conditions in terms of stem size, leaf area or biomass (Table 3). Only the root system exhibited some significant differences for the measured morphological parameters: inoculation of the rhizosphere with consortium 1 significantly enhanced total root projected area in comparison to control plants and inoculation with consortium 2. Consortium 1 increased mean root projected area by 5.7% relative to the uninoculated control. These measurements seem to confirm the PGP potential of this consortium composed of *Pseudomonas* and *Ensifer* strains, with a targeted impact on root development. In particular, strain UFC_B029 showed the highest IAA production *in vitro*, and genome-scale modelling also investigated the auxin production pathways in this strain.

3.8. Exploration of prospective metabolite exchanges or interspecies interactions within the selected bacterial consortia

Leveraging the metabolic models developed to study Hg resistance mechanisms and PGP compound production, the potential cross-feeding interactions within the three selected consortia were explored using community-scale simulations. Analysis of exchange flux distributions (Tables S2, S3 and S4) revealed several putative metabolite exchanges between community members, suggesting complementary metabolic capabilities and potential cooperative interactions within the consortia. These inferred exchanges reflect the metabolic potential predicted by the reconstructed community models under the imposed modelling constraints and environmental conditions considered in the simulations.

The first consortium was composed of *E. adhaerens* UFC_B030

Table 3
Morphological parameters measured on *S. aquatica grandis* seedlings after 6 weeks of cultivation following bacterial inoculation. For each parameter, the mean value ± the standard deviation is provided (n = 15). Letters indicate significant differences between conditions according to Kruskal-Wallis test followed by Dunn analysis ($p < 0.05$).

	Composition of the bacterial consortia			
	Control	**Consortium 1** *Ensifer* UFC_B030 + *Pseudomonas* UFC_B029 + *Pseudomonas* UFC_B037	**Consortium 2** *Pseudomonas* UFC_B023 + *Pseudomonas* UFC_B024 + *Pseudomonas* UFC_B028 + *Pseudomonas* UFC_B036	**Consortium 3** *Pseudomonas* UFC_B020 + *Pseudomonas* UFC_B021 + *Pseudomonas* UFC_B041
Total mass (g)	5.01 ± 1.66	5.18 ± 2.29	4.96 ± 2.10	3.79 ± 1.71
Stem size (cm)	27.7 ± 7.02	22.2 ± 7.23	23.5 ± 7.21	20.2 ± 7.84
Total leaf area (cm^2)	162.49 ± 54.37	144.15 ± 64.70	144.6 ± 61.33	112.7 ± 57.64
Total root length (cm)	319.96 ± 166.74	201.49 ± 149.29	366.89 ± 314.53	249.59 ± 241.67
Root projected area (cm^2)	448.83 ± 23.29 **a**	474.55 ± 7.52 **b**	456.88 ± 21.96 **a**	465.31 ± 9.73 **ab**

+ *P. frederiksbergensis* UFC_B029 + *P. jessenii* UFC_B037. In this community, L-arginine, guanine, uracil, and indole were predicted to be exchanged from *P. frederiksbergensis* UFC_B029 to *E. adhaerens* UFC_B030, suggesting a recurrent directional interaction between these two members. In addition, *E. adhaerens* UFC_B030 appeared as a potential donor of valine, hydrogen sulfide, and ethanol to *P. frederiksbergensis* UFC_B029 and *P. jessenii* UFC_B037, while ammonium was predicted to be exchanged from *P. jessenii* UFC_B037 to *E. adhaerens* UFC_B030. Altogether, the interaction profile of this consortium points to a combination of direct as well as indirect heavy-metal induced and quorum-associated metabolites that are linked to osmoprotection, sulfur metabolism, nitrogen assimilation, and anaerobic shifting (Table S11).

The second community was composed of *Pseudomonas sp.* UFC_B023 + *P. donghuensis* UFC_B028 + *P. putida* UFC_B024 + *Pseudomonas sp.* UFC_B036. The dominant exchange pattern in this consortium involved *Pseudomonas sp.* UFC_B023 and UFC_B036 as donors and UFC_B028 as a recurrent recipient. More specifically, *Pseudomonas sp.* UFC_B023 was predicted to supply arginine, uracil, and indole to *P. donghuensis* UFC_B028, whereas UFC_B036 was predicted to secrete leucine and valine to the same strain. In parallel, hydrogen sulfide was predicted to flow from *Pseudomonas sp.* UFC_B023 toward *P. putida* UFC_B024 and *Pseudomonas sp.* UFC_B036, and carbon monoxide from *P. putida* UFC_B024 to *Pseudomonas sp.* UFC_B036. Compared with the previous consortium, this community retained a wider representation of metabolites which were directly associated with stress-related functions and plant growth promotion, including arginine, indole, leucine, and valine. This could be attributed to the exchange network among the four microbes, which expands the space of feasible exchanges.

For the third consortium containing *P. baetica* UFC_B041 + *P. canadensis* UFC_B020 + *P. umsongensis* UFC_B021, the predicted interactions were dominated by only a few metabolites, namely hydrogen sulfide and formate from *P. umsongensis* UFC_B021 to *P. canadensis* UFC_B020, and carbon monoxide from *P. baetica* UFC_B041 to *P. canadensis* UFC_B020. Unlike the other two communities, no exchanges of indole, arginine, uracil, or other amino acid-related metabolites were predicted. Overall, this consortium displayed fewer metabolic interactions/exchanges that can be directly associated with heavy-metal induced stress tolerance or resistance mechanisms (Table S11).

4. Discussion

4.1. Genetic and phenotypic diversity of Hg resistance in rhizobacterial isolates

A total of 51 Hg-resistant rhizobacteria were isolated from chlor-alkali contaminated sediments, with an enrichment of the *Pseudomonas* genus. Previous studies have reported a high abundance of *Pseudomonas* in Hg-contaminated sites (Nakamura et al., 2001). Furthermore, numerous studies have focused on Hg resistance in *Pseudomonas*, confirming both the presence of genes from the *mer* operon and the effective capacity to biovolatilize Hg (Chang et al., 2021). For example, Bourdineaud et al. (2020) observed resistance of up to 80 μM of Hg^{2+} in *Pseudomonas idrijaensis*. Overall, the predominance of *Pseudomonas* isolates aligns with previous findings on Hg-contaminated sites, suggesting their ecological fitness for bioremediation applications.

Achromobacter and *Ensifer* genera have also been previously isolated from heavy metal-contaminated soils. For example, an *Achromobacter* strain isolated from a Cr-enriched environment exhibited resistance to multiple metals, including Cr, Ni, Cu and Zn (Oves et al., 2019). Previous works also demonstrated that some genes of the *mer* operon were found in an *Achromobacter* strain isolated from contaminated soil within a transposon, confirming the presence of resistance mechanisms within this genus (Ng et al., 2009). Regarding *Ensifer*, isolates have been detected in microbial communities from the Almadén mining district (Ciudad Real, Spain), one of the most heavily Hg contaminated environments worldwide. Moreover, *Ensifer* strains have been isolated from other Hg-enriched environments, such as legume nodules that were grown in contaminated soils (Nonnoi et al., 2012) and mercuric reductase activity encoded by the *merA* gene was detected in an *Ensifer* species (Arregui et al., 2021). MerA is a mercuric reductase that reduces Hg(II) to elemental Hg(0), rather than a general reductase for multiple metals (Christakis et al., 2021).

Consistent with the phenotypic variability observed among the isolates (Fig. 1), genome-scale modelling identified several genes associated with metal transport and homeostasis, including *fieF*, *copZ*, *zosA*, *silP*, and *zntA*. The reconstructed models also identified putative metal export reactions involving proton-coupled and ATP-dependent transport (Fig. 5**A**). While some of these genes are not directly linked to Hg detoxification, their known roles in metal transport and cellular homeostasis suggest that indirect or overlapping resistance mechanisms may contribute to the different Hg tolerance profiles observed across strains. Overall, within the same contaminated ecosystem, there were therefore different levels of resistance among bacterial communities, suggesting the co-existence of different mechanisms of tolerance to Hg.

4.2. Implications of PGP traits in Hg-resistant rhizobacteria for microbe-assisted phytoremediation

While Hg resistance is a critical adaptive trait in contaminated environments, the ability of rhizobacteria to promote plant growth is also an essential parameter for successful phytoremediation. Indeed, the co-occurrence of Hg resistance and PGP traits in the same isolates suggests a synergistic potential for both plant protection and soil decontamination. Among the bacterial isolates, certain strains stood out for their ability to produce molecules of interest for plant growth, such as IAA or siderophores, or to solubilise nutrients essential for plant development, such as phosphate. Several beneficial effects have been observed in host plants associated with IAA-producing endophytes, such as increased root growth, particularly for root hairs and lateral roots, and therefore an increased contact surface with the soil allowing an improved uptake of water and nutrients (Dimkpa et al., 2009). Moreover, the inoculation of siderophore-producing microorganisms into the rhizosphere can facilitate iron acquisition by plants, thereby promoting their growth, particularly in soils that have been altered by the presence of contaminants. Finally, phosphate solubilization capacity was measured as phosphorus tends to be rapidly immobilized in soils which can limit plant growth (Braud et al., 2015). Microorganisms capable of solubilizing phosphate make it more bioavailable, promoting plant development.

In this study, the results of the *in vitro* tests showed that, overall, all isolated strains demonstrated at least one PGP trait (Fig. 2; Table 2), and certain bacterial strains such as UFC_B020, UFC_B036, UFC_B039 or UFC_B041 appeared to be particularly promising for stimulating vegetation establishment, particularly in the context of soil contamination. This experimental evidence was further supported by *in silico* modelling, which identified biosynthetic pathways associated with PGP functions. In particular, the metabolic reconstruction of IAA production in UFC_B029 (Fig. 5**B**) aligns with *in vitro* observations, confirming its potential as a PGP bacterium. The predicted tryptophan-dependent pathway highlights the strain's capacity to synthesize and export IAA, while the identification of riboflavin biosynthetic pathway across all models (illustrated for UFC_B028 in Fig. 5**C**) suggests a fundamental role in microbial physiology, particularly in nutrient provisioning and redox metabolism. This pathway is highly conserved in bacteria and plants and involves flavin- and iron-sulfur-dependent intermediates linked to nutrient provisioning and redox metabolism in the rhizosphere (Bacher et al., 2001).

Species of the *Pseudomonas* genus are well known to display PGP traits such as the production of IAA, siderophores, or phosphate solubilization, both *in vitro* and in plant inoculation experiments (Rodríguez

et al., 2020). Furthermore, Kumar et al. (2018) also selected *Achromobacter xylosoxidans* among rhizospheric isolates, based on its numerous PGP traits. Another *Achromobacter* isolate showed the capacity to produce siderophore and IAA under heavy metal stress but no phosphate solubilization was observed (Mahale et al., 2024). Conversely, *Ensifer adhaerens* demonstrated an ability to solubilize phosphate, as well as other PGP traits such as the production of IAA, ammonium and several siderophores (Oves et al., 2017). This highlights that species, and even strains, within the same genus do not necessarily share the same PGP capacities. Such functional variability underlines the value of using microbial consortia, which can combine complementary traits (e.g., nutrient mobilization, phytohormone modulation, siderophore-mediated iron acquisition) and provide more robust, resilient benefits across diverse environmental conditions.

However, given the emergence of multi-resistant bacteria in recent years and the associated health risks, it is important to consider the presence of antibiotic resistance genes in isolated strains. In the case of Hg, a co-selection of antibiotic and Hg resistance genes has been observed several times (Priyadarshanee et al., 2021), since the latter may be carried by the same plasmids. In the One Health context (Pandey et al., 2023), care must be taken not to select strains that are multi-resistant to antibiotics as candidates for bioremediation and bioaugmentation approaches in order not to spread the associated resistance genes, especially in contaminated environments where existing selection pressure could make them persist. The susceptibility profiles provide useful preliminary information for biosafety evaluation. Further assessment prior to field application should consider mobile resistance and virulence determinants, horizontal gene transfer potential, and possible effects on resident microbial communities.

4.3. Genomic variation and functional patterns among bacterial isolates

The phenotypic diversity in Hg tolerance and PGP traits was accompanied by substantial genomic variation among the isolates. SNP and InDel profiles differed markedly among strains, both in their overall abundance and in the functional distribution of variant-associated genes (Fig. 3). As each isolate was compared with its corresponding reference genome, absolute variant numbers also reflect strain-to-reference divergence. Indeed, UFC_B030, UFC_B039 and UFC_B019 had the highest total SNP counts, whereas UFC_B020 and UFC_B021 showed the highest Hg tolerance. These contrasting patterns indicate that total variant burden alone is not closely associated with Hg tolerance and direct attention instead to the functional context of the affected genes.

Moreover, functional enrichment analysis revealed recurrent pathways related to variant-associated genes, including ABC transporters, two-component systems, or bacterial chemotaxis, whatever the type of variant considered (Fig. 4). ABC transporters are a family of membrane proteins that use ATP to transport various molecules, several of which have been identified as involved in metal transfer, which may explain the presence of genomic variations affecting the genes associated with these transporters (Theodoulou & Kerr, 2015). Moreover, two-component systems are composed of a homodimeric sensor histidine kinase and a response regulator that can bind to DNA and regulate the expression of certain genes in response to environmental changes (Casino et al., 2010). In addition, bacterial chemotaxis allows the detection of chemical gradients in the environment and can modify the motility of bacteria accordingly to optimize their position (Barrionuevo & Vullo, 2012). In the case of Hg-induced stress, this pathway can allow bacteria to migrate to a less contaminated area, with an avoidance strategy. Other studies have already observed that bacterial chemotaxis as well as the two-component systems were affected following Hg exposure in *Pseudomonas* isolates (Meyer et al., 2026).

Notably, transcriptomic analysis of UFC_B020 conducted in a previous study revealed a rapid upregulation of genes associated with metal detoxification and efflux pathways, independently of the *mer* operon (Meyer et al., 2026). This analysis identified differential expression in ABC transporters, thiol metabolism, and oxidative stress response systems, all of which are consistent with the variant-associated pathways described above. The upregulation of these pathways in UFC_B020 under Hg stress further supports the hypothesis that overlapping and compensatory mechanisms, including metal efflux, redox homeostasis, and signal transduction, contribute to Hg tolerance in rhizospheric bacteria.

Overall, these findings are consistent with the results of genome-scale modelling and phenotypic characterization. By identifying overlapping metal transport systems and conserved biosynthetic pathways, this approach identified candidates for further bioremediation testing of specific bacterial isolates. The integration of genomic and phenotypic data provides a robust framework for assessing microbial capabilities in environmental and biotechnological applications. Expression analyses and targeted functional tests of candidate transport and homeostasis genes will help resolve their contributions to the contrasting Hg tolerance profiles.

4.4. Validation of the potential of bacterial consortia on the promotion of *S. aquatica grandis*

To bridge the gap between *in vitro* characterization and field application, the PGP potential of three selected bacterial consortia was evaluated through *S. aquatica grandis* inoculation experiments, focusing on morphological measurements as key indicators of plant fitness: consortium 1 increased root projected area, although no significant biomass response was detected (Table 3). Indeed, the root system plays a crucial role in the absorption of water and nutrients that are required for proper plant growth, from the individual to the ecosystem. However, root architecture can be affected by several parameters in nature, including anthropic disturbances such as heavy metal pollution (Sharma et al., 2022). The enhancement of root architecture with the increase of root surface area following bacterial inoculation has already been described in previous studies (Vacheron et al., 2013). The work of Ashraf et al. (2017) gathered several studies where phytoremediation of heavy metals and plant growth was promoted by rhizospheric inoculation with microbial consortia or single bacteria. In particular, many of the species selected for their PGP characteristics belonged to the genus *Pseudomonas*, which is consistent with the results presented above. For instance, the inoculation with a *Pseudomonas* strain alleviated Hg-induced toxicity and reduced the uptake of Hg in the roots of wheat seedlings, further supporting the PGP potential of this genus (Chang et al., 2021). Regarding *Ensifer*, a few studies support the role of this genus in improving plant biomass yield, particularly *E. adhaerens*, either alone or within a consortium (Oves et al., 2019). In the presence of Hg contamination, *Ensifer medicae* exhibited a protective effect, limiting the stress induced by contamination on metabolic pathways in *Medicago truncatula* (Arregui et al., 2021). The work of Flores-Duarte et al. (2023) also demonstrated that the combination of two *Pseudomonas* species and two *Ensifer* species promoted *Medicago sativa* growth and nodulation in degraded estuarine soils under several abiotic stresses, including high metal contamination.

Inoculation with selected Hg-resistant bacterial consortia isolated from the study site promoted root development of *S. aquatica grandis* under the tested growth-chamber conditions, supporting their potential as plant-associated inoculants. The plant inoculation assay was conducted without Hg exposure and therefore cannot establish Hg-stress alleviation or remediation. In addition, the use of separate growth chambers for control and inoculated plants, together with the absence of a matched bacteria-free inoculum control, limits the attribution of the observed root response specifically to bacterial inoculation. Further evaluation under Hg exposure and more realistic soil conditions should combine plant performance with measurements of Hg partitioning in plant tissues and substrate, as well as volatilization where relevant. Subsequent non-sterile soil and field trials will also be important to determine the establishment and persistence of the introduced strains,

their interactions with resident microbial communities, and the stability of consortium performance across contrasting soil and seasonal conditions.

4.5. Deciphering metabolite exchange and prospective interspecies interactions from the metabolic models

Exposure to Hg can reshape carbon, nitrogen, and redox metabolism, promoting stress-adapted metabolic interactions and potential cross-feeding within microbial communities (Zheng et al., 2022). Consistent with this, genome-based flux predictions identified several small transportable metabolites across the three consortia, including arginine, leucine, valine, hydrogen sulfide, and ammonium, all previously associated with metal stress tolerance and resistance mechanisms. The community models yielded comparable predicted growth rates among members within each consortium (Table 1), while the predicted metabolite exchange profiles differed across the three communities. Several studies link arginine to plant-microbe and microbe-microbe interactions under metal toxicity, often *via* polyamine synthesis for stress tolerance (Cheng et al., 2021). In the study shown in Cheng et al. (2021), cadmium-resistant endophytic *Sphingomonas sp*. C40 produces arginine decarboxylase, converting arginine to a polyamine that reduces cadmium accumulation in rice plants. Regarding the interaction with leucine, Niu et al. (2021) showed that indigenous rhizosphere microbes produce leucine among the 410 metabolites in lead-stressed *Salix integra*, where it acts as a chelating agent. Evidence on valine in participating in stress tolerance/resistance mechanisms is scarce, however, it has been shown to act as alternate carbon/nitrogen source and desiccation/acid protectant under harsh metal-stressed conditions (Sze, 2022). Heavy metals decrease ammonia assimilation enzymes in plants, which can be mitigated by beneficial PGP microbes like *Rhizobium* and *Pseudomonas*, that enhance plant N-uptake efficiency by producing ammonia exogenously (Chi et al., 2025). Notably, ammonium exchange was predicted only in consortium 1, indicating a distinct nitrogen-sharing pattern within this community. This feature may contribute to functional differences among the consortia and provides a testable hypothesis in relation to the stronger root response observed with consortium 1. Except for ammonium and leucine that is present in first and the second community respectively, the rest of the metabolites are only being exchanged within consortia 1 & 2. Hydrogen sulfide exchange was predicted across all three consortia, pointing to sulfur metabolism as a shared feature of the modelled communities. Sulfur-related processes have been implicated in microbial responses to metal stress and in the regulation of iron homeostasis (Mao et al., 2025).

Amongst the metabolites that could be indirectly associated with metal-induced resistance and tolerance mechanisms are carbon monoxide, ethanol, formate, guanine, uracil and indole. Exposure to metals and the presence of anoxic conditions restructures microbial communities and redox metabolism by exerting oxidative stress. Consequently, this may enhance the extracellular production and exchange of those metabolites that could be used as an alternate carbon source, cell-signalling, or as a by-product of anaerobic pathways (Table S11). The predicted exchange of carbon monoxide could indicate a switch towards alternative carbon utilisation strategy under heavy metals stress and potentially anoxic rhizosphere microenvironments. This may suggest the activation of anaerobic carbon assimilation pathways under these conditions, although the simulations did not explicitly reproduce post-inoculation experimental conditions (Xu et al., 2025). However, the relevance of this interaction in the context of metal toxicity is still unknown. The production of ethanol and formate could also be a strategy to redistribute carbon in the presence of excessive reducing equivalents or oxidative stress (Gomez et al., 2018). The secretion of uracil and guanine, only visible for Community 1, might be beneficial for maintaining a high community growth rate as high uracil flux has been shown to redirect flux through the tricarboxylic acid cycle connecting to biomass synthesis (Fan et al., 2023). Indole, as a bacterial degradation product of tryptophan, could act as an intercellular signal in rhizosphere microbes, influencing quorum sensing, biofilm formation, and stress responses relevant to plant colonization (Hu et al., 2010). These predicted exchanges depend on the reconstructed metabolic networks and the constraints imposed during community modelling. As metabolite transfer was not directly measured, the simulations do not establish cross-feeding or cooperation among consortium members, nor do they confirm that the predicted ammonium exchange explains the root response observed with consortium 1. Direct metabolite measurements and strain-resolved co-culture experiments would be needed to test these predictions. Together, these model-derived exchange patterns identify metabolically distinct features among the three consortia and provide experimentally testable hypotheses for future co-culture and rhizosphere studies.

5. Conclusion

A total of 51 Hg-tolerant bacterial isolates were recovered from a chlor-alkali site, of which 16 were selected for detailed characterization. All 16 isolates exhibited at least one plant growth-promoting trait *in vitro*, and no phenotypic profile consistent with multidrug resistance was detected under the conditions tested. Their Hg tolerance varied considerably, with *P. canadensis* UFC_B020 and *P. umsongensis* UFC_B021 growing at 200 μM Hg, the highest concentration tested. However, the consortium containing these two isolates did not produce the strongest plant response. Instead, consortium 1 increased the root projected area of *S. aquatica grandis* by 5.7% relative to uninoculated controls after six weeks, without a significant increase in biomass. Genome-based analyses identified putative functions related to metal homeostasis and plant-associated metabolism, while community-scale modelling suggested potential metabolite exchanges that differed among the three consortia. These findings indicate that Hg tolerance alone is insufficient for selecting bacterial inoculants and highlight the importance of considering plant-associated functional traits and consortium performance. The willow inoculation assay was conducted without Hg exposure, and Hg uptake, transformation and removal were not assessed. Further studies should evaluate the selected consortia under Hg exposure, quantify Hg fate in plants and soil, validate the predicted metabolic functions and microbial interactions, and assess consortium persistence, performance and biosafety under more realistic soil and field conditions.

CRediT authorship contribution statement

Lorraine Meyer: Writing – review & editing, Writing – original draft, Methodology, Formal analysis, Data curation, Conceptualization. **Jun Zhou:** Writing – review & editing, Writing – original draft, Resources, Project administration, Methodology, Formal analysis, Data curation. **Stéphane Pfendler:** Writing – review & editing, Supervision, Resources, Methodology. **Akanksha Mishra:** Writing – review & editing, Writing – original draft, Resources, Methodology, Formal analysis, Data curation. **Lila Otero-Gonzalez:** Writing – review & editing, Resources, Project administration, Funding acquisition. **Marta Franco-Benito:** Writing – review & editing, Resources. **Sara Gil-Guerrero:** Writing – review & editing, Resources, Project administration. **Alexandre Meunier:** Writing – review & editing, Resources, Methodology. **Didier Hocquet:** Writing – review & editing, Resources, Methodology. **Stéphane Guyot:** Writing – review & editing, Supervision, Resources, Project administration. **Nicolas Capelli:** Writing – review & editing, Supervision, Resources, Project administration, Funding acquisition. **Michel Chalot:** Writing – review & editing, Supervision, Resources, Project administration, Funding acquisition.

Funding sources

The project BIOSYSMO has received funding from the European Union's Horizon Europe research and innovation program under grant

agreement n°101060211. This work has been supported by TRANSBIO Graduate School (contract ANR-15-IDEX-0003) and the Region Bourgogne-Franche-Comté.

Declaration of Competing Interest

The authors declare that they have no known competing financial interests or personal relationships that could have appeared to influence the work reported in this paper.

Acknowledgements

We would like to express our sincere thanks to the PEA²t platform (Université Marie et Louis Pasteur, Chrono-environnement, F-25000 Besançon, France) for technical support. We gratefully thank Frédéric Grenouillet for assisting us with the use of MALDI-TOF MS.

Appendix A. Supporting information

Supplementary data associated with this article can be found in the online version at doi:10.1016/j.ecoenv.2026.120984.

Data availability

Data will be made available on request.

References

Arregui, G., Hipólito, P., Pallol, B., Lara-Dampier, V., García-Rodríguez, D., Varela, H.P., Zaniani, P.T., Balomenos, D., Paape, T., De la Peña, T.C., Lucas, M.M., Pueyo, J.J., 2021. Mercury-tolerant ensifer medicae strains display high mercuric reductase activity and a protective effect on nitrogen fixation in Medicago truncatula nodules under mercury stress. Front. Plant Sci. 11. https://doi.org/10.3389/fpls.2020.560768.

Ashraf, M.A., Hussain, I., Rasheed, R., Iqbal, M., Riaz, M., Arif, M.S., 2017. Advances in microbe-assisted reclamation of heavy metal contaminated soils over the last decade: a review. J. Environ. Manag. 198, 132–143. https://doi.org/10.1016/j.jenvman.2017.04.060.

Bacher, A., Eberhardt, S., Eisenreich, W., Fischer, M., Herz, S., Illarionov, B., Kis, K., Richter, G., 2001. Biosynthesis of riboflavin. Vitam. Horm. 61, 1. https://doi.org/10.1016/s0083-6729(01)61001-x.

Barbier, F., Wolff, M., 2010. Multirésistance chez Pseudomonas aeruginosa. Médecine/Sci. 26 (11), 960–968. https://doi.org/10.1051/medsci/20102611960.

Barbosa, L.O., Lima, J.S., Magalhães, V.C., Gava, C.A.T., Soares, A.C.F., Marbach, P.A.S., De Souza, J.T., 2018. Compatibility and combination of selected bacterial antagonists in the biocontrol of sisal bole rot disease. BioControl 63 (4), 595–605. https://doi.org/10.1007/s10526-018-9872-x.

Barrionuevo, M.R., Vullo, D.L., 2012. Bacterial swimming, swarming and chemotactic response to heavy metal presence: which could be the influence on wastewater biotreatment efficiency. World J. Microbiol. Biotechnol. 28 (9), 2813–2825. https://doi.org/10.1007/s11274-012-1091-5.

Becerra-Castro, C., Prieto-Fernández, A., Álvarez-Lopez, V., Monterroso, C., Cabello-Conejo, M.I., Acea, M.J., Kidd, P.S., 2011. Nickel Solubilizing Capacity and Characterization of Rhizobacteria Isolated from Hyperaccumulating and Non-Hyperaccumulating Subspecies of Alyssum serpyllifolium. Int. J. Phytoremediat. 13 (sup1), 229–244. https://doi.org/10.1080/15226514.2011.568545.

Bourdineaud, J., Durn, G., Režun, B., Manceau, A., Hrenović, J., 2020. The chemical species of mercury accumulated by Pseudomonas idrijaensis, a bacterium from a rock of the Idrija mercury mine, Slovenia. Chemosphere 248, 126002. https://doi.org/10.1016/j.chemosphere.2020.126002.

Braud, A., Hubert, M., Gaudin, P., Lebeau, T., 2015. A quick rhizobacterial selection tests for the remediation of copper contaminated soils. J. Appl. Microbiol. 119 (2), 435–445. https://doi.org/10.1111/jam.12865.

Casino, P., Rubio, V., Marina, A., 2010. The mechanism of signal transduction by two-component systems. Curr. Opin. Struct. Biol. 20 (6), 763–771. https://doi.org/10.1016/j.sbi.2010.09.010.

Chang, J., Yan, Z., Dong, J., Wu, X., Meng, Z., Shi, Y., Chen, J., 2021. Mechanisms controlling the transformation of and resistance to mercury(II) for a plant-associated Pseudomonas sp. strain, AN-B15. J. Hazard. Mater. 425, 127948. https://doi.org/10.1016/j.jhazmat.2021.127948.

Cheng, C., Wang, R., Sun, L., He, L., Sheng, X., 2021. Cadmium-resistant and arginine decarboxylase-producing endophytic Sphingomonas sp. C40 decreases cadmium accumulation in host rice (Oryza sativa Cliangyou 513). Chemosphere 275, 130109. https://doi.org/10.1016/j.chemosphere.2021.130109.

Chi, Y., Ma, X., Chu, S., You, Y., Chen, X., Wang, J., Wang, R., Zhang, X., Zhang, D., Zhao, T., Zhang, D., Zhou, P., 2025. Nitrogen cycle induced by plant growth-promoting rhizobacteria drives “microbial partners” to enhance cadmium phytoremediation. Microbiome 13 (1), 113. https://doi.org/10.1186/s40168-025-02113-x.

Christakis, C.A., Barkay, T., Boyd, E.S., 2021. Expanded diversity and phylogeny of mer genes broadens mercury resistance paradigms and reveals an origin for MerA among thermophilic Archaea. Front. Microbiol. 12. https://doi.org/10.3389/fmicb.2021.682605.

Ciadamidaro, L., Parelle, J., Tatin-Froux, F., Moyen, C., Durand, A., Zappelini, C., Morin-Crini, N., Soupe, D., Blaudez, D., Chalot, M., 2019. Early screening of new accumulating versus non-accumulating tree species for the phytomanagement of marginal lands. Ecol. Eng. 130, 147–156. https://doi.org/10.1016/j.ecoleng.2019.02.010.

Collot, J., Binet, P., Arsenov, D., Chalot, M., 2026. Tolerance and trace elements extraction of Alliaria petiolata and Salix aquatica grandis under increased Cd(II) and Zn(II) exposure. Ecotoxicol. Environ. Saf. 314, 120074. https://doi.org/10.1016/j.ecoenv.2026.120074.

Diener, C., Gibbons, S.M., Resendis-Antonio, O., 2020. MICOM: metagenome-scale modeling to infer metabolic interactions in the gut microbiota. mSystems 5 (1). https://doi.org/10.1128/msystems.00606-19.

Dimkpa, C., Weinand, T., Asch, F., 2009. Plant–rhizobacteria interactions alleviate abiotic stress conditions. Plant Cell Environ. 32 (12), 1682–1694. https://doi.org/10.1111/j.1365-3040.2009.02028.x.

Dworkin, M., Foster, J.W., 1958. Experiments with some microorganisms which utilize ethane and hydrogen. J. Bacteriol. 75 (5), 592–603. https://doi.org/10.1128/jb.75.5.592-603.1958.

Fan, L., Pan, Z., Liao, X., Zhong, Y., Guo, J., Pang, R., Chen, X., Ye, G., Su, Y., 2023. Uracil restores susceptibility of methicillin-resistant Staphylococcus aureus to aminoglycosides through metabolic reprogramming. Front. Pharmacol. 14, 1133685. https://doi.org/10.3389/fphar.2023.1133685.

Flores-Duarte, N.J., Navarro-Torre, S., Mateos-Naranjo, E., Redondo-Gómez, S., Pajuelo, E., Rodríguez-Llorente, I.D., 2023. Nodule Synthetic Bacterial Community as Legume Biofertilizer under Abiotic Stress in Estuarine Soils. Plants 12 (11), 2083. https://doi.org/10.3390/plants12112083.

François, F., Lombard, C., Guigner, J., Soreau, P., Brian-Jaisson, F., Martino, G., Vandervennet, M., Garcia, D., Molinier, A., Pignol, D., Peduzzi, J., Zirah, S., Rebuffat, S., 2011. Isolation and characterization of environmental bacteria capable of extracellular biosorption of Mercury. Appl. Environ. Microbiol. 78 (4), 1097–1106. https://doi.org/10.1128/aem.06522-11.

Frank, J.A., Reich, C.I., Sharma, S., Weisbaum, J.S., Wilson, B.A., Olsen, G.J., 2008. Critical evaluation of two primers commonly used for amplification of bacterial 16S rRNA genes. Appl. Environ. Microbiol. 74 (8), 2461–2470. https://doi.org/10.1128/AEM.02272-07.

Gang, S., Sharma, S., Saraf, M., Buck, M., Schumacher, J., 2019. Analysis of indole-3-acetic acid (IAA) production in Klebsiella by LC-MS/MS and the Salkowski method. BIO-Protoc. 9 (9). https://doi.org/10.21769/bioprotoc.3230.

Gomez, J.A.L., Mukhopadhya, I., Duncan, S.H., Louis, P., Shaw, S., Collie-Duguid, E., Crost, E., Juge, N., Flint, H.J., 2018. Formate cross-feeding and cooperative metabolic interactions revealed by transcriptomics in co-cultures of acetogenic and amylolytic human colonic bacteria. Environ. Microbiol. 21 (1), 259–271. https://doi.org/10.1111/1462-2920.14454.

Hu, M., Zhang, C., Mu, Y., Shen, Q., Feng, Y., 2010. Indole affects biofilm formation in bacteria. Indian. J. Microbiol. 50 (4), 362–368. https://doi.org/10.1007/s12088-011-0142-1.

Kumar, A., Vyas, P., Kumar, D., Dubey, A., 2018. Screening and Characterization of Achromobacter xylosoxidans isolated from rhizosphere of Jatropha curcas L. (Energy Crop) for plant-growth-promoting traits. J. Adv. Res. Biotechnol. 3 (1), 1. https://doi.org/10.15226/2475-4714/3/1/00134.

Kumar, A.G., Manisha, D., Rajan, N.N., Sujitha, K., Peter, D.M., Kirubagaran, R., Dharani, G., 2023. Biodegradation of phenanthrene by piezotolerant Bacillus subtilis EB1 and genomic insights for bioremediation. Mar. Pollut. Bullet. 194, 115151. https://doi.org/10.1016/j.marpolbul.2023.115151.

Machado, D., Andrejev, S., Tramontano, M., Patil, K.R., 2018. Fast automated reconstruction of genome-scale metabolic models for microbial species and communities. Nucleic Acids Res. 46 (15), 7542–7553. https://doi.org/10.1093/nar/gky537.

Mahale, M., Samson, R., Dharne, M., Kodam, K., 2024. Harnessing the potential of Achromobacter sp. M1 to remediate heavy metals from wastewater: genomic insights and environmental applications. J. Hazard. Mater. 480, 136125. https://doi.org/10.1016/j.jhazmat.2024.136125.

Mao, C., Jin, W., Xiang, Y., Zhu, Y., Wu, J., Liu, X., Wu, S., Qiao, W., Cheung, K.M.C., Yeung, K.W.K., 2025. Biosynthesis of H 2 S and Siderophores Targeting Gram-Negative Bacterial Resistance to Reactive Oxygen Species. Adv. Sci. 12 (45), e05748. https://doi.org/10.1002/advs.202505748.

Meyer, L., Guyot, S., Chalot, M., Capelli, N., 2023. The potential of microorganisms as biomonitoring and bioremediation tools for mercury-contaminated soils. Ecotoxicol. Environ. Saf. 262, 115185. https://doi.org/10.1016/j.ecoenv.2023.115185.

Meyer, L., Zhou, J., Pfendler, S., Mei, S., Wang, M., Capelli, N., Guyot, S., Chalot, M., 2026. Characterization and transcriptome analysis of mercury-resistant Pseudomonas canadensis isolated from a chlor-alkali contaminated soil revealed mer-independent detoxification pathways. J. Hazard. Mater. Adv. 21, 101069. https://doi.org/10.1016/j.hazadv.2026.101069.

Nakamura, K., Iwahara, M., Furukawa, K., 2001. Screening of organomercurial-volatilizing bacteria in the mercury-polluted sediments and seawater of Minamata Bay in Japan. Clean. Prod. Process. 3 (2), 104–107. https://doi.org/10.1007/s100980100107.

Nautiyal, C., 1999. An efficient microbiological growth medium for screening phosphate solubilizing microorganisms. FEMS Microbiol. Lett. 170 (1), 265–270. https://doi.org/10.1016/s0378-1097(98)00555-2.

Ng, S., Davis, B., Palombo, E.A., Bhave, M., 2009. A Tn5051-like mer-containing transposon identified in a heavy metal tolerant strain Achromobacter sp. AO22. BMC Res. Notes 2 (1), 38. https://doi.org/10.1186/1756-0500-2-38.

Niu, X., Wang, S., Zhou, J., Di, D., Sun, P., Huang, D., 2021. Inoculation With Indigenous Rhizosphere Microbes Enhances Aboveground Accumulation of Lead in Salix integra Thunb. by Improving Transport Coefficients. Front. Microbiol. 12, 686812. https://doi.org/10.3389/fmicb.2021.686812.

Nonnoi, F., Chinnaswamy, A., De la Torre, V.S.G., De la Peña, T.C., Lucas, M.M., Pueyo, J.J., 2012. Metal tolerance of rhizobial strains isolated from nodules of herbaceous legumes (Medicago spp. and Trifolium spp.) growing in mercury-contaminated soils. Appl. Soil. Ecol. 61, 49–59. https://doi.org/10.1016/j.apsoil.2012.06.004.

Oves, M., Khan, M.S., Qari, H.A., 2017. Ensifer adhaerens for heavy metal bioaccumulation, biosorption, and phosphate solubilization under metal stress condition. J. Taiwan. Inst. Chem. Eng. 80, 540–552. https://doi.org/10.1016/j.jtice.2017.08.026.

Oves, M., Khan, M.S., Qari, H.A., 2019. Chromium-reducing and phosphate-solubilizing Achromobacter xylosoxidans bacteria from the heavy metal-contaminated soil of the Brass city, Moradabad, India. Int. J. Environ. Sci. Technol. 16 (11), 6967–6984. https://doi.org/10.1007/s13762-019-02300-y.

Pandey, S., Doo, H., Keum, G.B., Kim, E.S., Kwak, J., Ryu, S., Choi, Y., Kang, J., Kim, S., Lee, N.R., Oh, K.K., Lee, J., Kim, H.B., 2023. Antibiotic resistance in livestock, environment and humans: One Health perspective. J. Anim. Sci. Technol. 66 (2), 266–278. https://doi.org/10.5187/jast.2023.e129.

Priyadarshanee, M., Chatterjee, S., Rath, S., Dash, H.R., Das, S., 2021. Cellular and genetic mechanism of bacterial mercury resistance and their role in biogeochemistry and bioremediation. J. Hazard. Mater. 423, 126985. https://doi.org/10.1016/j.jhazmat.2021.126985.

Rice, K.M., Walker, E.M., Wu, M., Gillette, C., Blough, E.R., 2014. Environmental Mercury and Its Toxic Effects. J. Prev. Med. Public Health 47 (2), 74–83. https://doi.org/10.3961/jpmph.2014.47.2.74.

Rodríguez, M., Torres, M., Blanco, L., Béjar, V., Sampedro, I., Llamas, I., 2020. Plant growth-promoting activity and quorum quenching-mediated biocontrol of bacterial phytopathogens by Pseudomonas segetis strain P6. Sci. Rep. 10 (1). https://doi.org/10.1038/s41598-020-61084-1.

Santos, I.C., Hildenbrand, Z.L., Schug, K.A., 2016. Applications of MALDI-TOF MS in environmental microbiology. Analyst 141 (10), 2827–2837. https://doi.org/10.1039/c6an00131a.

Schwyn, B., Neilands, J., 1987. Universal chemical assay for the detection and determination of siderophores. Anal. Biochem. 160 (1), 47–56. https://doi.org/10.1016/0003-2697(87)90612-9.

Sharma, A., Kapoor, D., Gautam, S., Landi, M., Kandhol, N., Araniti, F., Ramakrishnan, M., Satish, L., Singh, V.P., Sharma, P., Bhardwaj, R., Tripathi, D.K., Zheng, B., 2022. Heavy metal induced regulation of plant biology: recent insights. Physiol. Plant 174 (3). https://doi.org/10.1111/ppl.13688.

Sze, H.W., 2022. Distribution of soil heavy metals across ecologically distinct habitats on Signy island, maritime Antarctica and its association with bacterial community composition and metabolic profiles (Doctoral dissertation). International Medical University.

Theodoulou, F.L., Kerr, I.D., 2015. ABC transporter research: going strong 40 years on. Biochem. Soc. Trans. 43 (5), 1033–1040. https://doi.org/10.1042/bst20150139.

Vacheron, J., Desbrosses, G., Bouffaud, M., Touraine, B., Moënne-Loccoz, Y., Muller, D., Legendre, L., Wisniewski-Dyé, F., Prigent-Combaret, C., 2013. Plant growth-promoting rhizobacteria and root system functioning. Front. Plant Sci. 4. https://doi.org/10.3389/fpls.2013.00356.

Xu, J., Bravo, A.G., Lagerkvist, A., Bertilsson, S., Sjöblom, R., Kumpiene, J., 2014. Sources and remediation techniques for mercury contaminated soil. Environ. Int. 74, 42–53. https://doi.org/10.1016/j.envint.2014.09.007.

Xu, Y., Teng, Y., Liao, J., Leung, P.M., Dai, S., Sun, Y., Hu, W., Wang, H., Li, Y., Huang, Y., Guo, Z., Pan, X., Dong, X., Luo, Y., Greening, C., 2025. Carbon monoxide exposure stimulates growth and activity of primary producers in diverse soil ecosystems. Environ. Sci. Technol. 59 (33), 17581–17594. https://doi.org/10.1021/acs.est.5c02881.

Zappelini, C., Karimi, B., Foulon, J., Lacercat-Didier, L., Maillard, F., Valot, B., Blaudez, D., Cazaux, D., Gilbert, D., Yergeau, E., Greer, C., Chalot, M., 2015. Diversity and complexity of microbial communities from a chlor-alkali tailings dump. Soil. Biol. Biochem. 90, 101–110. https://doi.org/10.1016/j.soilbio.2015.08.008.

Zhang, B., Li, P., Wang, Y., Wang, J., Liu, X., Wang, X., Hu, X., 2021. Characterization and synthesis of indole-3-acetic acid in plant growth promoting Enterobacter sp. RSC Adv. 11 (50), 31601–31607. https://doi.org/10.1039/d1ra05659j.

Zheng, X., Cao, H., Liu, B., Zhang, M., Zhang, C., Chen, P., Yang, B., 2022. Effects of Mercury contamination on microbial diversity of different kinds of soil. Microorganisms 10 (5), 977. https://doi.org/10.3390/microorganisms10050977.